IEEE Access
Multidisciplinary | Rapid Review | Open Access Journal

Received January 3, 2020, accepted January 15, 2020, date of publication February 3, 2020, date of current version February 12, 2020.

*Digital Object Identifier 10.1109/ACCESS.2020.2971317*

# Viscoelasticity of Rubber Springs Affects Vibration Characteristics of a Flip-Flow Screen With the High G Value

**JIAN TANG, LINKAI NIU, XIAOYAN XIONG, AND SHIJUN JIE**

Key Laboratory of Advanced Transducers and Intelligent Control System, Ministry of Education, Taiyuan University of Technology, Taiyuan 030024, China

Corresponding author: Xiaoyan Xiong (xiongxy7070@163.com)

This work was supported in part by the National Natural Science Foundation of China under Grant 51775364, and in part by the Shanxi Talented Person Project under Grant 201705D211009.

**ABSTRACT** With the high G value of vibration, outstanding sieving behaviors of a flip-flow screen are more likely to appear, but structural damages are aggravated under the high amplitude vibration. Considering rubber springs role on the vibration energy dissipation, viscoelasticity of rubber springs (i.e., shear springs and vibration isolation springs), is noticed to deal with the above contradiction. However, when rubber springs experience large amplitude vibration, viscoelastic responses influence more on the amount of damping than in the linear (i.e., small amplitude) vibration regime, as the frequency dependence of rubber springs is noteworthy. For this purpose, the Generalized Maxwell model is used to depict the frequency dependence of rubber springs and the practical damping is converted to a series damping parameters of the system, numerical models of the flip-flow screen under startup and shutdown modes and steady working conditions are proposed and verified firstly. Secondly, in order to explore kinetics responses of the elastic screen panel under different rubber springs damping coefficients, nonlinear finite element model of which is established. Finally, effects of rubber springs nonlinear damping on screen frames vibrations and screen panels nonlinear responses are studied. Results indicate that hysteretic damping of rubber springs can effectively solve the conflict between vibration strength and structural reliability of the flip-flow screen, since the low sensitivities of maximum stresses and the high sensitivities of accelerations to rubber springs damping are found.

**INDEX TERMS** Viscoelastic damping, frequency dependence, generalized Maxwell model, nonlinear responses, flip-flow screen, vibration intensity.

## I. INTRODUCTION

Relying on the intense alternating load generated by the rotation of the vibration exciter and engaged reciprocating motions of the elastic screen surface, acceleration of a flip-flow screen is nearly 50 g, which makes difficult-to-filter coal easy pass through screen pores [1]. However, with the high amplitude vibration, sustaining coupling load effects (e.g., the imposed alternating load, the inertial load of the screen body and the impact load of the screen surface) on the flip-flow screen are increased, which result in aggravating structural damages of the equipment [2]. Thus, a reasonable vibration strength is of critical importance for dealing with the contradiction.

Structural reliability is mainly affected by the vibration intensity of the screen body [3]. Under a certain excitation force, the dynamic characteristics of the screen body is regulated by vibration energy dissipation of rubber springs (i.e., shear springs and vibration isolation springs). Excellent screening efficiency of a flip-flow screen relies on the ejection intensity of the screen surface whose boundary conditions are accord with vibrations of the screen body. Thus, the contradiction between screening efficiency and structural reliability can be resolved by viscoelastic damping of rubber springs.

The motion of the screen body can be decomposed into several components along different directions in the coordinate system. Then, dynamic characteristics of the screen

The associate editor coordinating the review of this manuscript and approving it for publication was Ludovico Minati.

body are probed by solving vibration differential equations of the screen system, which are established based on the vibration theory [4], [5]. Considering degrees of freedom in the translation and rotation, 1-DOF [6], uncoupled 2-DOF [7], coupled 3-DOF [8]–[10] and spatial 3-DOF model [11]–[13] are adopted. From the standpoint of engineering applicability, the 2-DOF model is the most commonly implemented one in dynamic analyses.

Shear springs and vibration isolation springs, which are made of the rubber material exhibit substantial viscoelastic behaviors. Usually, their nonlinear behaviors are described by modifying the classical linear viscoelastic constitutive model (e.g., Kevin-Voigt model and Maxwell model) and establishing the constitutive model [14], [15]. Three different general forms which adopted are as follows. One is to consider the higher-order time function, which contains multiple higher-order time derivatives of stress and strain in the constitutive relation. Secondly, the method of introducing the concept of convolution is applied. Furthermore, new concepts, such as internal variables in the field of thermodynamics, are used to establish the constitutive model [16]–[20]. However, because vibration amplitudes of the flip-flow screen are influenced by its vibration frequency, large vibration amplitude of rubber springs, especially shear springs, exist in the working process[21], the Kelvin-Voigt model is not sufficient to capture hysteretic damping characteristics of rubber springs as the relaxation time changes with the varying vibration amplitudes [22], [23].

In order to depict the nonlinear damping of shear springs, Gong [24] raised a nonlinear shear spring model based on the superposition of elastic force, friction force and fractional derivative force to describe the nonlinear behavior effects of the shear springs on flip-flow screen kinetics. Yuan *et al.* [25] regarded rubber springs as the isotropic structure and gave the corresponding material attributes. By the finite element method, stress and displacement distributions of flip-flow screen frames were obtained by instantaneous dynamics analyses.

In this paper, hysteretic damping (where stiffness and damping are represented together by a complex spring) is used extensively to describe the dissipation presents in viscoelastic systems as the Generalized Maxwell model consisted of the static spring and several Maxwell cells is introduced in. Then, the model, which takes account of frequency dependency of rubber springs, is transformed into a non-integer derivative to solve motions of the two screen frames under startup and shutdown modes.

In addition, the screen surface consisted of several screen panels is another critical nonlinear component of the flip-flow screen. With the nonlinear material and the large deflection in the screening process, nonlinear dynamics of the screen surface largely affect the screening performance. Generally, dynamic analyses of the screen panel are based on two types of models. One is by the linearized method. Through considering the screen panel as an elastic press rod [26], [27], a slender compressible bar [28] and a simply-supported beam [29],

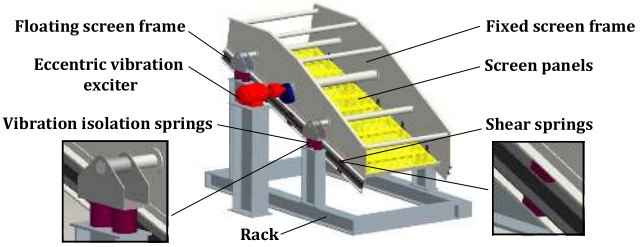


**FIGURE 1.** The structure of the flip-flow screen.

respectively, the motion of the screen panel is investigated. In light of the inclined angle, a mathematical model of the inclined screen panel is established based on the Catenary theory in [7]. With the model, deflection forms of the screen panel are obtained. Zhang makes a further improvement based on the model. In [30], [31], the flexible screen panel is discretized into several rigid strips. Then, according to vertical displacement forms of the screen panel, the rigid strips are assembled into an approximate flexible screen panel, and motions of the screen panel are simulated in line with the theory of multiple body dynamics. The other method is based on the nonlinear FEM. Using the Mooney-Rivlin material model, hyper-elastic properties of the screen panel are performed [32]. Then dynamic distributions of the screen panel are computed by the explicit algorithm [33]. Yet, researches above mainly focus on influences of self-parameters and installation characteristics of the screen surface, the mass of the screen body and excitation forces on dynamic responses of the screen panel, which neglect effects of rubber springs (including shear springs and vibration isolation springs) dynamic characteristics. Because of the importance of rubber springs nonlinearity, with the established nonlinear finite element model of the screen panel, independent and coupling effects of the shear spring and the vibration isolation spring are discussed in this paper.

## II. MODEL CONSTRUCTIONS

The higher ejection acceleration of the flip-flow screen derives from motions of elastic screen surfaces. As shown in FIGURE 1, a fixed screen frame beam is arranged between two floating screen frame beams. Thus the two ends of the screen panel can be mounted on the fixed screen frame and the floating screen frame, respectively. The rotation of the eccentric vibration exciter provides a simple harmonic vibration with screen frames. The fixed screen frame, which is mounted on the rack through vibration isolation springs, connects with the floating screen frame by shear springs. Due to the different inertial forces of the two screen frames, different vibration phases appear in them, which results in periodical slack and stretch motions of the elastic screen panel. Then, under the projectile behavior of the screen surface, sieving materials can achieve the high ejection acceleration of 50g [1].

### A. VIBRATION MODEL OF THE SCREEN BODY

During the startup and the shutdown periods, vibration amplitudes of the flip-flow screen change with varying excitation frequencies. As respond amplitudes of shear springs equal to

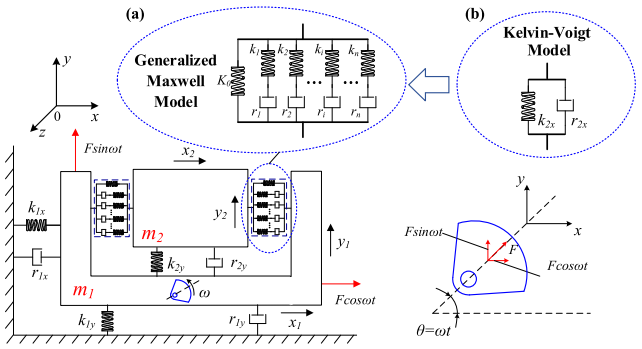


(a) Under startup and shutdown modes
(b) Under steady working conditions

**FIGURE 2.** Numerical model of the screen body.

amplitude differences between the two screening frames, hysteretic damping as well as dynamic stiffness of shear spring present frequency dependency [24], especially in the main vibration direction ($x$ direction). For this situation, the Generalized Maxwell model, which leads to a close dynamic behavior of the non-integer derivative, is used to better reflect the nonlinear damping characteristics of shear springs along $x$ direction. Since the amplitude differences of the flip-flow screen are small along y direction and vibration isolation springs work in its linear regime, the Kelvin-Voigt model is sufficient to capture their damping.

As shown in FIGURE 2, the angular velocity of the eccentric blocks is $\omega$. So, the angle between the line of excitation force and $x$ axis is $\omega$, and the two components of the excitation force $F$ along $x$ direction and $y$ direction can be written as

$$\begin{cases} F_x = F\cos\theta = F\cos\omega t \\ F_y = F\sin\theta = F\sin\omega t \end{cases} \tag{1}$$

Then, the vibration differential equation of the flip-flow screen along $x$ direction can be written as

$$\begin{cases} m_1\ddot{x}_1 + r_{1x}\dot{x}_1 + k_{1x}x_1 + f = F\cos\omega t \\ m_2\ddot{x}_2 - f = 0 \end{cases} \tag{2}$$

where $f$ is the nonlinear force of shear springs along $x$ direction.

The behavior of the shear spring in the frequency domain approached to that of a non-integer derivative and can be expressed by the following transfer function:

$$G(s) = \frac{f}{x} = K_0 + C\cdot s^{\beta} \tag{3}$$

where $K_0$ is the static stiffness of the shear spring, $C$ is the damping coefficient, $s$ is the Laplace variable, $\beta$ is the non-integer number.

According to above complex representations of mechanical impedance, the total dynamic stiffness and total phase of the shear spring at the frequency of $f_i$ can be written as

$$\begin{aligned} \left|{}^{f}\!/_{X}\,(j\omega_i)\right| &= \left|K_i + jK_i\tan(\varphi_i)\right| \\ &= \sqrt{K_i^2 + \left(K_i\tan\left(\varphi_i\pi/180\right)\right)^2} \end{aligned} \tag{4}$$

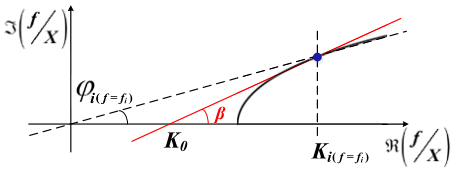


**FIGURE 3.** Nyquist diagram of the Generalized Maxwell model.

where $K_{i(f=f_i)}$ and $\varphi_{i(f=f_i)}$ are the dynamic stiffness and phase of the shear spring measured at the frequency of $f_i$ (in FIGURE 3). The typical transfer function can be plotted in the Nyquist diagram.

Because the fractional transfer function is an irrational function, which can't be directly realized. A direct idea is to approximate the irrational transfer function with a higher-order rational transfer function (e.g., traditional integer order transfer function).

The Generalized Maxwell model leads to a close dynamic behavior of the non-integer derivator. With the static spring (spring of stiffness $K_0$) and several Maxwell cells (in parallel spring $k_i$ and damper $r_i$), the general form of the Generalized Maxwell model is given in (5) with the relaxation time of $\tau_i = r_i/k_i$,

$$\begin{aligned} &\sigma + \sum_{n=1}^{N}\left(\sum_{i_1=1}^{N-n+1}\cdots\left(\sum_{i_a=i_{a-1}+1}^{N-(n-a)+1}\cdots\left(\sum_{i_n=i_{n-1}+1}^{N}\right.\right.\right. \\ &\left.\left.\left.\times\left(\prod_{j\in\{i_1,\cdots,i_n\}}\tau_j\right)\right)\cdots\right)\cdots\right)\frac{\partial^n\sigma}{\partial t^n} = E_0\varepsilon \\ &+\sum_{n=1}^{N}\left(\sum_{i_1=1}^{N-n+1}\cdots\left(\sum_{i_a=i_{a-1}+1}^{N-(n-a)+1}\cdots\left(\sum_{i_n=i_{n-1}+1}^{N}\right.\right.\right. \\ &\left.\left.\left.\times\left(\left(E_0+\sum_{j\in\{i_1,\cdots,i_n\}}E_j\right)\left(\prod_{k\in\{i_1,\cdots,i_n\}}\tau_k\right)\right)\right)\cdots\right)\cdots\right)\frac{\partial^n\varepsilon}{\partial t^n} \end{aligned} \tag{5}$$

and the total dynamic stiffness can be expressed in as

$$\begin{aligned} G(s) = \frac{f}{x} = K_0 &+ \frac{r_1\cdot k_1\cdot s}{r_1\cdot s + k_1} \\ &+ \frac{r_2\cdot k_2\cdot s}{r_2\cdot s + k_2} + \ldots + \frac{r_n\cdot k_n\cdot s}{r_n\cdot s + k_n} \end{aligned} \tag{6}$$

Transfer function in (7) is given to approximate dynamic stiffness expression in (6) which asymptotes has a slope of 6dB/oct to approximate a slope lower than 6dB/oct.

$$\begin{aligned} G(s) = K_0 &+ \frac{K_{01}\cdot(\tau_{n1}\cdot s+1)\cdot(\tau_{n2}\cdot s+1)\cdot\ldots\cdot(\tau_{nn}\cdot s+1)}{(\tau_{d1}\cdot s+1)\cdot(\tau_{d2}\cdot s+1)\cdot\ldots\cdot(\tau_{dn}\cdot s+1)} \end{aligned} \tag{7}$$

where $K_{01}$ is an additional static stiffness (not physical) which lead by the mathematical determination.

Zeroes and poles of the transfer function in (7) can be computed based on the "Oustaloup" algorithm[34].

Given a frequency range $[\omega_b, \omega_h]$, the zero and the pole of rank $i$ can be written as

$$\omega_i' = \omega_b \left(\omega_h / \omega_b\right)^{\frac{i+N+0.5(1-\beta)}{2N+1}} = 1/\tau_{ni} \tag{8}$$

and

$$\omega_i = \omega_b \left(\omega_h / \omega_b\right)^{\frac{i+N+0.5(1+\beta)}{2N+1}} = 1/\tau_{di} = k_i/r_i \tag{9}$$

where $\beta \in R^+$ is the fractional order, $\tau_{ni}$ and $\tau_{di}$ are differentiation time constants, $2N+1$ is the number of zeros or poles.

Each parameter of (7)-(9) can be calculated according to the following relations:

$$\omega_0 = \gamma^{0.5}\omega_u \text{ and } \omega_0' = \gamma^{-0.5}\omega_u \tag{10}$$

$$(\omega_b\ \omega_h)^{0.5} = \omega_u \tag{11}$$

$$K_{01} = \left(\omega_b/\omega_u\right)^{\beta} = \left(\omega_u/\omega_h\right)^{\beta} \tag{12}$$

$$\omega_{-N}' = \eta^{0.5}\omega_b \text{ and } \omega_N = \eta^{-0.5}\omega_h \tag{13}$$

$$\omega_{i+1}'/\omega_i' = \omega_{i+1}/\omega_i = \gamma\eta > 1 \tag{14}$$

$$\omega_{i+1}'/\omega_i = \eta > 0 \text{ and } \omega_i/\omega_i' = \gamma > 0 \tag{15}$$

$$\beta = \log\gamma / \log(\gamma\eta) \tag{16}$$

The ratio $\gamma$ and $\eta$ are defined by (15).

After that, rewriting the transfer function in (7) with partial fractions as

$$G(s) = \frac{e}{x} = K_0 + K_{01} + \sum_{i=1}^{N} \frac{A_i}{1 + s/\omega_i} \tag{17}$$

with

$$A_i = \left[\left(1 + s/\omega_i\right) G(s)\right]_{s=-\omega_i} \tag{18}$$

and

$$K_{01} = G(\infty) = \left(\omega_b/\omega_h\right)^{\beta} \prod_{i=1}^{N} \frac{\omega_i}{\omega_i'} \tag{19}$$

In this way, the dynamic stiffness of the shear spring which modelled by the Generalized Maxwell model in the time domain can be given as:

$$f = g(t) = (K_0 + K_{01})\delta(t) + \sum_{i=1}^{N} A_i\omega_i e^{-\omega_i t} u(t) \tag{20}$$

where $\delta(t)$ and $u(t)$ are the unit impulse and step.

When the flip-flow screen works in steady working conditions, the vibration amplitude of the shear spring is a constant value. So the Kelvin-Voigt model is used to describe the viscoelasticity of rubber springs (including shear springs and vibration isolation springs).

The vibration differential equation of the flip-flow screen along $x$ direction and $y$ direction can be simplified as

$$\begin{cases} m_1\ddot{x}_1 + r_{1x}\dot{x}_1 + k_{1x}x_1 + r_{2x}(\dot{x}_1 - \dot{x}_2) + k_{2x}(x_1 - x_2) \\ \qquad = F\cos\omega t \\ m_1\ddot{y}_1 + r_{1y}\dot{y}_1 + k_{1y}y_1 + r_{2y}(\dot{y}_1 - \dot{y}_2) + k_{2y}(y_1 - y_2) \\ \qquad = F\sin\omega t \\ m_2\ddot{x}_2 - r_{2x}(\dot{x}_1 - \dot{x}_2) - k_{2x}(x_1 - x_2) = 0 \\ m_2\ddot{y}_2 - r_{2y}(\dot{y}_1 - \dot{y}_2) - k_{2y}(y_1 - y_2) = 0 \end{cases} \tag{21}$$

where $m_1$ and $m_2$ are masses of the fixed screen frame and the floating screen frame, respectively. $x_1$ and $x_2$ are displacements of the fixed screen frame and the floating screen frame along $x$ direction, respectively. $y_1$ and $y_2$ are displacements of the fixed screen frame and the floating screen frame along $y$ direction, respectively. $\dot{x}_1$ and $\dot{x}_2$ are velocities of the fixed screen frame and the floating screen frame along $x$ direction, respectively. $\dot{y}_1$ and $\dot{y}_2$ are velocities of the fixed screen frame and the floating screen frame along $y$ direction, respectively. $\ddot{x}_1$ and $\ddot{x}_2$ are accelerations of the fixed screen frame and the floating screen frame along $x$ direction, respectively. $\ddot{y}_1$ and $\ddot{y}_2$ are accelerations of the fixed screen frame and the floating screen frame along $y$ direction, respectively. $k_{1x}$ and $k_{1y}$ are stiffness of vibration isolation springs along $x$ direction and $y$ direction, respectively. $k_{2x}$ and $k_{2y}$ are the stiffness of shear springs along $x$ direction and $y$ direction, respectively. $r_{1x}$ and $r_{1y}$ are damping of vibration isolation

$$\begin{cases} x_1 = F \cdot \dfrac{k_{2x} - m_2\omega^2 + r_{2x}i\omega}{\left(k_{1x} - m_1\omega^2\right)\left(k_{2x} - m_2\omega^2\right) + \left(-k_{2x}m_2 + r_{2x}^2 - r_{1x}r_{2x}\right)\omega^2 + \left(k_{2x} - m_2\omega^2\right)r_{1x}i\omega + \left(k_{1x} - k_{2x} - m_1\omega^2\right)r_{2x}i\omega} \\ x_2 = F \cdot \dfrac{k_{2x} + r_{2x}i\omega}{\left(k_{1x} - m_1\omega^2\right)\left(k_{2x} - m_2\omega^2\right) + \left(-k_{2x}m_2 + r_{2x}^2 - r_{1x}r_{2x}\right)\omega^2 + \left(k_{2x} - m_2\omega^2\right)r_{1x}i\omega + \left(k_{1x} - k_{2x} - m_1\omega^2\right)r_{2x}i\omega} \\ y_1 = F \cdot \dfrac{k_{2y} - m_2\omega^2 + r_{2y}i\omega}{\left(k_{1y} - m_1\omega^2\right)\left(k_{2y} - m_2\omega^2\right) + \left(-k_{2y}m_2 + r_{2y}^2 - r_{1y}r_{2y}\right)\omega^2 + \left(k_{2y} - m_2\omega^2\right)r_{1y}i\omega + \left(k_{1y} - k_{2y} - m_1\omega^2\right)r_{2y}i\omega} \\ y_2 = F \cdot \dfrac{k_{2y} + r_{2y}i\omega}{\left(k_{1y} - m_1\omega^2\right)\left(k_{2y} - m_2\omega^2\right) + \left(-k_{2y}m_2 + r_{2y}^2 - r_{1y}r_{2y}\right)\omega^2 + \left(k_{2y} - m_2\omega^2\right)r_{1y}i\omega + \left(k_{1y} - k_{2y} - m_1\omega^2\right)r_{2y}i\omega} \end{cases} \tag{23}$$

springs along $x$ direction and $y$ direction, respectively, $r_{2x}$ and $r_{2y}$ are damping of shear springs along $x$ direction and $y$ direction, respectively.

The excitation force in FIGURE 2 can be represented by the complex vector as $Fe^{i\omega t}$. Then, solutions of (21) can be written as

$$\begin{cases} x_1 = A_1 e^{i(\omega t-\psi_1)} \\ x_2 = A_2 e^{i(\omega t-\psi_1)} \\ y_1 = B_1 e^{i(\omega t-\varphi_1)} \\ y_2 = B_2 e^{i(\omega t-\varphi_2)} \end{cases} \tag{22}$$

where $A_1$ and $A_2$ are displacement amplitudes of the fixed screen frame and the floating screen frame along $x$ direction, respectively, $\psi_1$ and $\psi_2$ are displacement phases of the fixed screen frame and the floating screen frame along $x$ direction, respectively, $B_1$ and $B_2$ are displacement amplitudes of the fixed screen frame and the floating screen frame along $y$ direction, respectively, $\varphi_1$ and $\varphi_2$ are displacement phases of the fixed screen frame and the floating screen frame along $y$ direction, respectively.

Thus, complex representations of displacements can be obtained according to (21) and (22) as (23), shown at the bottom of the previous page.

Therefore, displacement amplitudes of the fixed screen frame and the floating screen frame along $x$ direction and $y$ direction are (24), as shown at the bottom of this page.

Then, displacement phases of the fixed screen frame and the floating screen frame along $x$ direction and $y$ direction can be written as (25), shown at the bottom of this page.

In order to investigate damping influences of the shear springs and the vibration isolation springs, related damping coefficients are extracted as follows: $z_x = r_{1x}/r_{2x}$, $\xi_x = r_{2x}/r_{cx}$, $r_{cx} = 2m_2P_{1x}$, $P_{1x} = \sqrt{k_{1x}/m_1}$, $p_{2x} = \sqrt{k_{2x}/m_2}$, $\alpha_x = P_{2x}/P_{1x}$, $\lambda_x = \omega/P_{1x}$, $z_y = r_{1y}/r_{2y}$, $\xi_y = r_{2y}/r_{cy}$, $r_{cy} = 2m_2P_{1y}$, $P_{1y} = \sqrt{k_{1y}/m_1}$, $P_{2y} = \sqrt{k_{2y}/m_2}$, $\alpha_y =$

$$\begin{cases} A_1 = F \cdot \sqrt{\dfrac{\left(k_{2x}-m_2\omega^2\right)^2 + r_{2x}^2\omega^2}{\left[\left(k_{1x}-m_1\omega^2\right)\left(k_{2x}-m_2\omega^2\right) + \left(-k_{2x}m_2 + r_{2x}^2 - r_{1x}r_{2x}\right)\omega^2\right]^2 + \left[\left(k_{2x}-m_2\omega^2\right)r_{1x}\omega + \left(k_{1x}-k_{2x}-m_1\omega^2\right)r_{2x}\omega\right]^2}} \\ A_2 = F \cdot \sqrt{\dfrac{k_{2x}^2 + r_{2x}^2\omega^2}{\left[\left(k_{1x}-m_1\omega^2\right)\left(k_{2x}-m_2\omega^2\right) + \left(-k_{2x}m_2 + r_{2x}^2 - r_{1x}r_{2x}\right)\omega^2\right]^2 + \left[\left(k_{2x}-m_2\omega^2\right)r_{1x}\omega + \left(k_{1x}-k_{2x}-m_1\omega^2\right)r_{2x}\omega\right]^2}} \\ B_1 = F \cdot \sqrt{\dfrac{\left(k_{2y}-m_2\omega^2\right)^2 + r_{2y}^2\omega^2}{\left[\left(k_{1y}-m_1\omega^2\right)\left(k_{2y}-m_2\omega^2\right) + \left(-k_{2y}m_2 + r_{2y}^2 - r_{1y}r_{2y}\right)\omega^2\right]^2 + \left[\left(k_{2y}-m_2\omega^2\right)r_{1y}\omega + \left(k_{1y}-k_{2y}-m_1\omega^2\right)r_{2y}\omega\right]^2}} \\ B_2 = F \cdot \sqrt{\dfrac{k_{2y}^2 + r_{2y}^2\omega^2}{\left[\left(k_{1y}-m_1\omega^2\right)\left(k_{2y}-m_2\omega^2\right) + \left(-k_{2y}m_2 + r_{2y}^2 - r_{1y}r_{2y}\right)\omega^2\right]^2 + \left[\left(k_{2y}-m_2\omega^2\right)r_{1y}\omega + \left(k_{1y}-k_{2y}-m_1\omega^2\right)r_{2y}\omega\right]^2}} \end{cases} \tag{24}$$

$$\begin{cases} \psi_1 = \arctan \dfrac{\left[\left(k_{1x}-m_1\omega^2\right)\left(k_{2x}-m_2\omega^2\right) + \left(-k_{2x}m_2 + r_{2x}^2 - r_{1x}r_{2x}\right)\omega^2\right]r_{2x}\omega}{\left[\left(k_{1x}-m_1\omega^2\right)\left(k_{2x}-m_2\omega^2\right) + \left(-k_{2x}m_2 + r_{2x}^2 - r_{1x}r_{2x}\right)\omega^2\right]\left(k_{2x}-m_2\omega^2\right) + \left[\left(k_{2y}-m_2\omega^2\right)r_{1x}\omega + \left(k_{1x}-k_{2x}-m_1\omega^2\right)r_{2x}\omega\right]} \\ \psi_2 = \arctan \dfrac{\left[\left(k_{1x}-m_1\omega^2\right)\left(k_{2x}-m_2\omega^2\right) + \left(-k_{2x}m_2 + r_{2x}^2 - r_{1x}r_{2x}\right)\omega^2\right]r_{2x}\omega}{\left[\left(k_{1x}-m_1\omega^2\right)\left(k_{2x}-m_2\omega^2\right) + \left(-k_{2x}m_2 + r_{2x}^2 - r_{1x}r_{2x}\right)\omega^2\right]k_{2x} + \left[\left(k_{2x}-m_2\omega^2\right)r_{1x}\omega + \left(k_{1x}-k_{2x}-m_1\omega^2\right)r_{2x}\omega\right]r_{2x}\omega} \\ \varphi_1 = \arctan \dfrac{\left[\left(k_{1y}-m_1\omega^2\right)\left(k_{2y}-m_2\omega^2\right) + \left(-k_{2y}m_2 + r_{2y}^2 - r_{1y}r_{2y}\right)\omega^2\right]r_{2y}\omega}{\left[\left(k_{1y}-m_1\omega^2\right)\left(k_{2y}-m_2\omega^2\right) + \left(-k_{2y}m_2 + r_{2y}^2 - r_{1y}r_{2y}\right)\omega^2\right]\left(k_{2y}-m_2\omega^2\right) + \left[\left(k_{2y}-m_2\omega^2\right)r_{1y}\omega + \left(k_{1y}-k_{2y}-m_1\omega^2\right)r_{2y}\omega\right]} \\ \varphi_2 = \arctan \dfrac{\left[\left(k_{1y}-m_1\omega^2\right)\left(k_{2y}-m_2\omega^2\right) + \left(-k_{2y}m_2 + r_{2y}^2 - r_{1y}r_{2y}\right)\omega^2\right]r_{2y}\omega}{\left[\left(k_{1y}-m_1\omega^2\right)\left(k_{2y}-m_2\omega^2\right) + \left(-k_{2y}m_2 + r_{2y}^2 - r_{1y}r_{2y}\right)\omega^2\right]k_{2y} + \left[\left(k_{2y}-m_2\omega^2\right)r_{1y}\omega + \left(k_{1y}-k_{2y}-m_1\omega^2\right)r_{2y}\omega\right]r_{2y}\omega} \end{cases} \tag{25}$$

$P_{2y}/P_{1y}$, $\lambda_y = \omega/P_{1y}$, $\mu = m_2/m_1$, where $z_x$ and $z_y$ are relative damping of vibration isolation springs to shear springs along $x$ and $y$ direction, respectively. $\xi_x$ and $\xi_y$ are the damping ratio along $x$ and $y$ direction, respectively. $r_{cx}$ and $r_{cy}$ are the critical damping of the flip-flow screen along $x$ and $y$ direction, respectively. $P_{1x}$ and $P_{2x}$ are natural frequencies of the fixed screen frame and the floating screen frame along $x$ direction, respectively. $P_{1y}$ and $P_{2y}$ are natural frequencies of the fixed screen frame and the floating screen frame along $y$ direction, respectively. $\alpha_x$ and $\alpha_y$ are natural frequency ratios of the fixed screen frame to the floating screen frame along $x$ and $y$ direction, respectively. $\lambda_x$ and $\lambda_y$ are ratios of the rotation frequency to the resonance frequency along $x$ and $y$ direction. $\mu$ is the mass ratio of the fixed screen frame to the floating screen frame.

In this way, displacement amplitudes of the fixed screen frame and the floating screen frame along $x$ direction and $y$ direction can be written as (26), shown at the bottom of this page.

In this scection, according to the established model, dynamic responses of the screen body are caluculated in AMESim as shown in FIGURE 4.

### B. NONLINEAR FEM MODEL OF THE SCREEN PANEL

The screen panel is another nonlinear element of the flip-flow screen, which is made of polyurethane. Polyurethane is a kind of incompressible hyper-elastic material with nonlinear properties (e.g., its large strain can be produced with the small stress). Meanwhile, under the periodical slack and stretch motions, large deformations of the whole screen panel appear, which lead to nonlinear behaviors of the screen surface in the working process.

Nonlinear dynamic characteristics of the large deformed screen surface is investigated by nonlinear FEM. For two ends of the screen panel are fixed on screen frames, its boundary

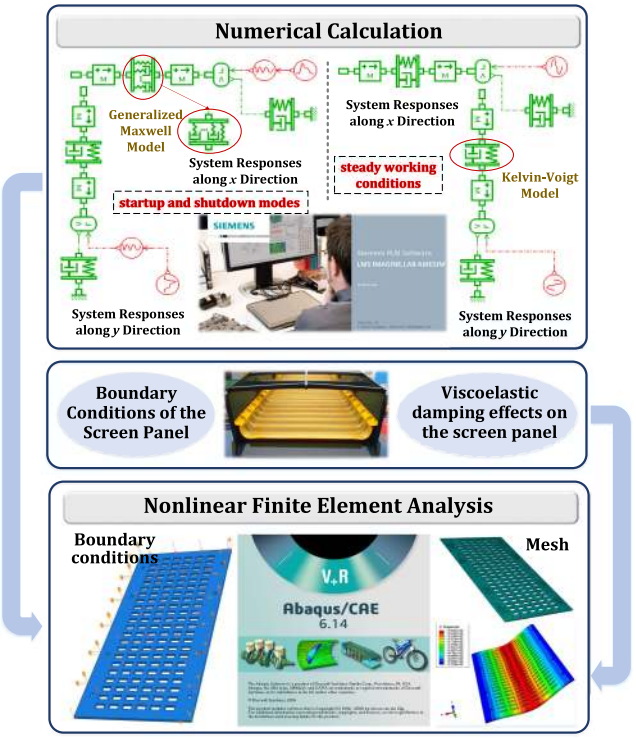


**FIGURE 4.** Schematic diagram of the nonlinear analysis.

conditions consistent with motions of the two screen frames. Uniform loads caused by weights of material groups and impact loads induced by the collision of screening coals are imposed on the screen surface. Loads of the screen surface are equivalent to its normal pressure [35], [36]. Thus, the normal pressure of a single screen panel can be written as

$$P = m(g + \alpha)/A \tag{27}$$

where $m$ is the mass of screening material, $\alpha$ is the collision acceleration between particles and the screen surface and $A$ is

$$\begin{cases} A_1 = \dfrac{F}{k_{1x}} \sqrt{\dfrac{\left(\alpha_x^2 - \lambda_x^2\right)^2 + (2\xi_x\lambda_x)^2}{\left[\left(\lambda_x^2 - 1\right)\left(\lambda_x^2 - \alpha_x^2\right) - \mu\left(\lambda_x^2\alpha_x^2 + (z_x - 1)(2\xi_x\lambda_x)^2\right)\right]^2 + (2\xi_x\lambda_x)^2\left[1 - \lambda_x^2 + \mu\left((z_x - 1)\alpha_x^2 - \lambda_x^2\right)\right]^2}} \\ A_2 = \dfrac{F}{k_{1x}} \sqrt{\dfrac{\alpha_x^2 + (2\xi_x\lambda_x)^2}{\left[\left(\lambda_x^2 - 1\right)\left(\lambda_x^2 - \alpha_x^2\right) - \mu\left(\lambda_x^2\alpha_x^2 + (z_x - 1)(2\xi_x\lambda_x)^2\right)\right]^2 + (2\xi_x\lambda_x)^2\left[1 - \lambda_x^2 + \mu\left((z_x - 1)\alpha_x^2 - \lambda_x^2\right)\right]^2}} \\ B_1 = \dfrac{F}{k_{1y}} \sqrt{\dfrac{\left(\alpha_y^2 - \lambda_y^2\right)^2 + (2\xi_y\lambda_y)^2}{\left[\left(\lambda_y^2 - 1\right)\left(\lambda_y^2 - \alpha_y^2\right) - \mu\left(\lambda_y^2\alpha_y^2 + (z_y - 1)(2\xi_y\lambda_y)^2\right)\right]^2 + (2\xi_y\lambda_y)^2\left[1 - \lambda_y^2 + \mu\left((z_y - 1)\alpha_y^2 - \lambda_y^2\right)\right]^2}} \\ B_2 = \dfrac{F}{k_{1y}} \sqrt{\dfrac{\alpha_y^2 + (2\xi_y\lambda_y)^2}{\left[\left(\lambda_y^2 - 1\right)\left(\lambda_y^2 - \alpha_y^2\right) - \mu\left(\lambda_y^2\alpha_y^2 + (z_y - 1)(2\xi_y\lambda_y)^2\right)\right]^2 + (2\xi_y\lambda_y)^2\left[1 - \lambda_y^2 + \mu\left((z_y - 1)\alpha_y^2 - \lambda_y^2\right)\right]^2}} \end{cases} \tag{26}$$

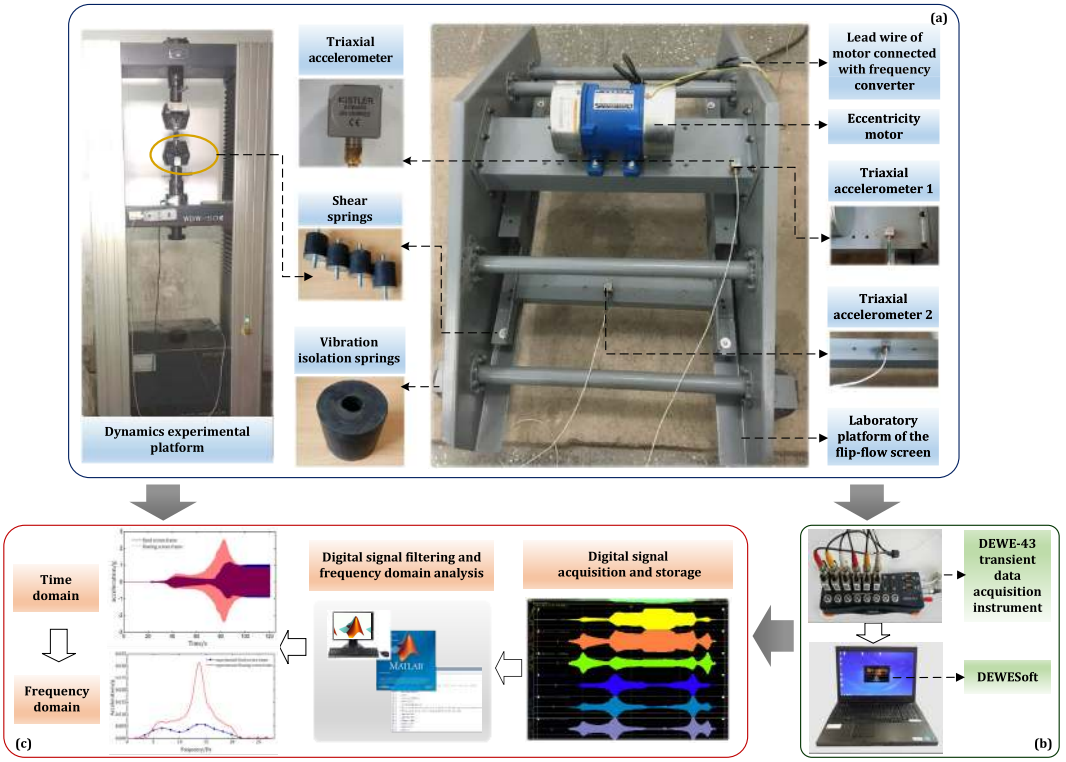


**FIGURE 5.** The scheme of the acceleration measurement experiment.

the sieving area. When the capacity of the screening equals to $18t/h$, the normal pressure of the screen surface is 425.78Pa.

The Mooney-Rivlin model in (28) is used to fitting hyper-elastic material behaviors of the screen panel.

$$U = Coef\ (1) \times \left(\bar{I}_1 - 3\right) + Coef\ (2) \times \left(\bar{I}_2 - 3\right) + (J-1)/D_1 \quad (28)$$

where $U$ is the strain energy potential of polyurethane, $\bar{I}_1$ and $\bar{I}_2$ are the first and second strain invariants that is used to describe torsional properties of polyurethane, $Coef\,(1)$ and $Coef\,(2)$ are used to describe shear properties of polyurethane and $(J-1)/D_1$ is used to describe the compressibility of polyurethane. Material parameters of the polyurethane are shown in Table 1.

Nonlinear dynamic responses of the screen panel are solved by explicit calculation method. In the solving process, mesh distortions will occur due to the large deflection of the screen panel. Thus, the analysis cannot continue. In order to enhance the numerical convergence, mesh reconstruction method is adopted by mapping data of mesh nodes. In this way, nonlinear deformations of the screen panel can be computed through the model.

## III. EXPERIMENTAL VERIFICATION

In this section, an experiment of the flip-flow screen is carried out to validate the constructed model in Sect II. The scheme of the experiment is illustrated in FIGURE 5. During the experiment, time-domain responses of the flip-flow screen were sampled. Then, with Fast Fourier Transform (FFT), frequency-domain responses were obtained. Finally, the measurement results were compared with the simulation results to verify the accuracy of the model.

The laboratory platform of the flip-flow screen is shown in FIGURE 5(b). The basic parameters of the platform are shown in Table 2. The excitation frequency of the flip-flow

**TABLE 1.** Material properties of polyurethane.

| Mass Density ($kg/m^3$) | Shore Hardness | Coef(1) (Pa) | Coef(2) (Pa) | $D_1(m^2/N)$ |
|---|---|---|---|---|
| 1200 | 70 | 460000 | 120000 | $10^{-6}$ |

**TABLE 2.** Basic parameters of the experimental flip-flow screen.

| Parameters | Units | Values |
|---|---|---|
| Maximum length of the screen | mm | 1.200 |
| Maximum width of the screen | mm | 0.840 |
| Maximum height of the screen | mm | 0.775 |
| Mass of the fixed screen frame | Kg | 69.257 |
| Mass of the floating screen frame | Kg | 9.686 |
| Total static stiffness of vibration isolation springs | N/m | 140000 |
| Total static stiffness of shear springs | N/m | 60000 |
| Damping ratio | / | 0.03 |
| Relative damping | / | 12 |

screen depends on the rotation speed of the eccentric vibration exciter, which was controlled by a SANKEN EF-0.75K frequency converter. In order to keep the excitation frequency consisted with the working frequency of the flip-flow screen, the sweeping range was set to 0-25Hz. Two KISTLER 8795A50 triaxial accelerometers were mounted on the vibration exciter beam and the floating screen beam respectively, which were used to measure accelerations of the fixed screen frame and the floating screen frame. The KISTLER 8795A50 triaxial accelerometer is allowed to measure the signal whose frequency range from 1Hz to 4 kHz with a high resolution of 1mg and sensibility of 100mV/g. The dynamic range of the acceleration is ±50g. The *x, y* and *z* axis of the triaxial accelerometers are accord with the coordinate system in FIGURE 2.

DEWE-43 transient data acquisition device equipped with eight AD24-bit dynamic acquisition channels is shown in FIGURE 5(b). During the process of vibration signal acquisition, the triaxial accelerometers were connected to the transient data acquisition device through couplers, and the transient data acquisition device was connected to the computer. To ensure the acquired data completely describes the real-time acceleration signals, the sampling frequency was set to 1,000 Hz, which was far higher than the maximum vibration frequency. Moreover, the Blackman window was used in the FFT algorithm to reduce the spectrum leakage. However, amplitudes in frequency-domain responses would be slightly influenced by the window function.

Acceleration curves of the flip-flow screen under the startup mode obtained by the simulation and the experiment are shown in FIGURE 6. It can be found in FIGURE 6(a) and FIGURE 6(b) that the total simulation sampling time is 6 s while the whole experimental sampling time is 120 s. This is because the continuous transform speed of the eccentric vibration exciter was given by the speed function in the simulation, but that was achieved by the manual regulation of the transducer in the experiment. However, the difference of the sampling time will not affect the time-domain analysis and the frequency-domain analysis of the flip-flow screen.

Compared to responses of the flip-flow screen in FIGURE 6(c) and FIGURE 6(d), frequency-domain responses of the fixed screen frame and the floating screen frame in the simulation are accord with that in the experiment. There are two peak-to-peak points in each frequency spectrum, which agree with resonance frequencies of the flip-flow screen. At the same time, different acceleration amplitudes between the two frequency spectrums are found, which are caused by different total frequency sampling points and the remained spectrum leakage.

In addition, resonance frequencies and corresponding acceleration amplitudes of the screen are listed in Table 3. Meanwhile, calculated errors of the above parameters between the simulation and the experiment are less than 5 %. Hence, the reasonability of the model of the startup mode in Sect II is proved.

**TABLE 3. Resonance frequencies and corresponding acceleration amplitudes of the flip-flow screen along x direction.**

| Items | Resonance frequencies(Hz) | | Acceleration amplitudes(g) | |
|---|---|---|---|---|
| | First | Second | Fixed screen frame | Floating screen frame |
| Simulation | 6.499 | 13.199 | 0.368 / 0.952 | 0.515 / 2.561 |
| Experiment | 6.320 | 13.430 | 0.351 / 0.993 | 0.490 / 2.551 |
| Errors/% | 2.754 | 1.750 | 4.620 / 4.307 | 4.854 / 0.400 |

Acceleration curves of the flip-flow screen obtained by the simulation and the experiment under the steady working condition are shown in FIGURE 7. When the flip-flow screen worked in the near-resonant region at the frequency about 13 Hz (marked regions in FIGURE 6(a) and FIGURE 6 (b)), phase differences between the fixed screen frame and the floating screen frame that obtained by the simulation and the experiment are 114.55° and 113.23°, respectively. The error between the two results is 1.15%.

In order to investigate deviations between the simulation results and the experimental results, 101 evenly distributed points of every acceleration curves in FIGURE 7 were sampled, respectively. Then corresponding descriptive and correlational analyses were conducted.

According to (29), Pearson's product moment correlation coefficient between the simulation curve and the experimental curve of the fixed screen frame is 0.99807 and that of the floating screen frame is 0.99886. For all of them are more than 0.8, there is a strong linear relationship between the simulation results and the experimental results. Thus, movements of the fixed screen frame and the floating screen frame under the steady working condition can be well described by the model of (21) in Sect II.

$$\rho_{x,y} = \frac{cov\,(X, Y)}{\sigma_x \sigma_y} = \frac{E\,((X - E\,(X))\,(Y - E\,(Y)))}{\sigma_x \sigma_y} \quad (29)$$

where $\sigma_x$ and $\sigma_y$ are standard deviations of the two compared variables, $E()$ denotes the expected value of the variable and $cov()$ means covariance.

## IV. RESULTS AND DISCUSSION

Through the numerical calculation, responses of the flip-flow screen body and dynamics of the large deformed screen panel in steady working processes have been obtained. In Sect A and B, rubber springs damping effects on responses of the screen body and the nonlinear screen panel are investigated. Then, regression analysis of damping effects are given in Sect C. Finally, sensitivity analyses of damping to kinetic parameters of the screen panel are proposed in Sect D.

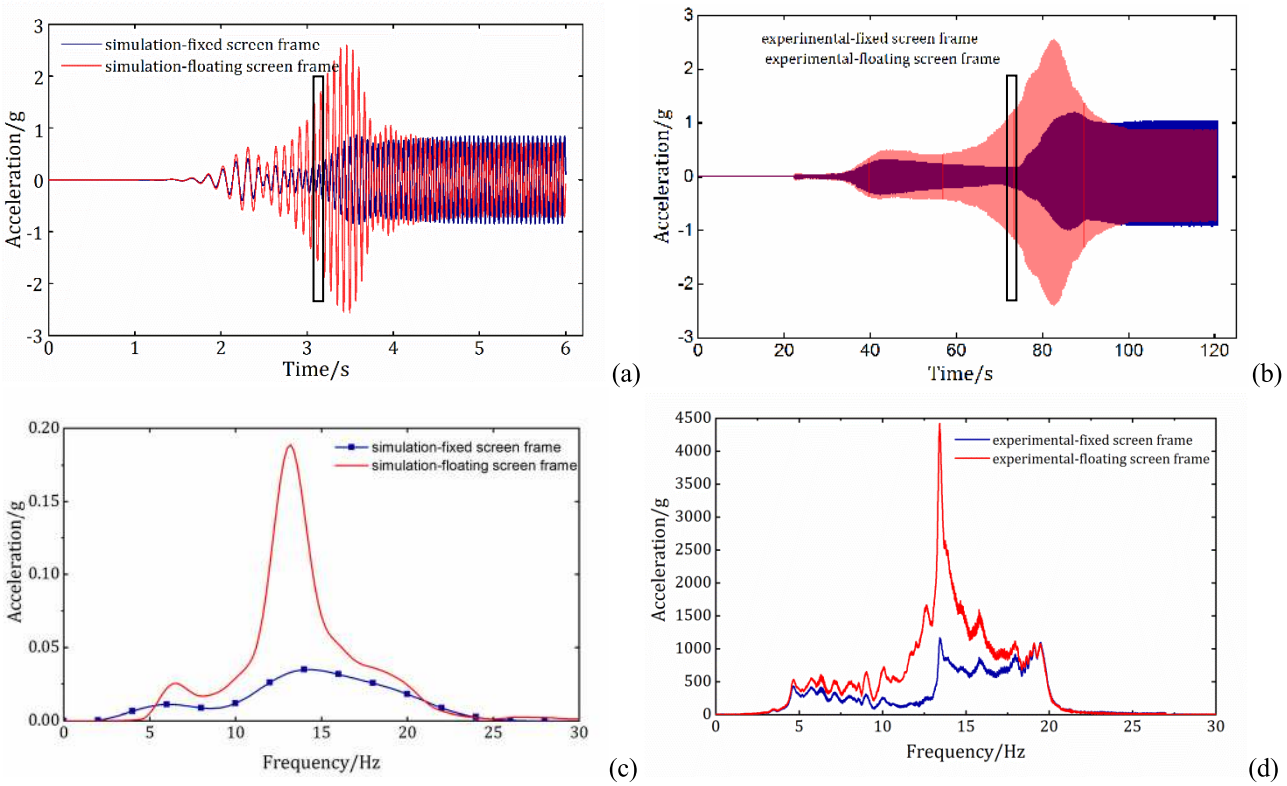


(a) Time-domain responses along x direction obtained by the simulation
(b) Time-domain responses along x direction obtained by the experiment
(c) Frequency-domain responses along x direction obtained by the simulation
(d) Frequency-domain responses of along x direction obtained by the experiment

**FIGURE 6.** Acceleration responses of the flip-flow screen under the startup mode.

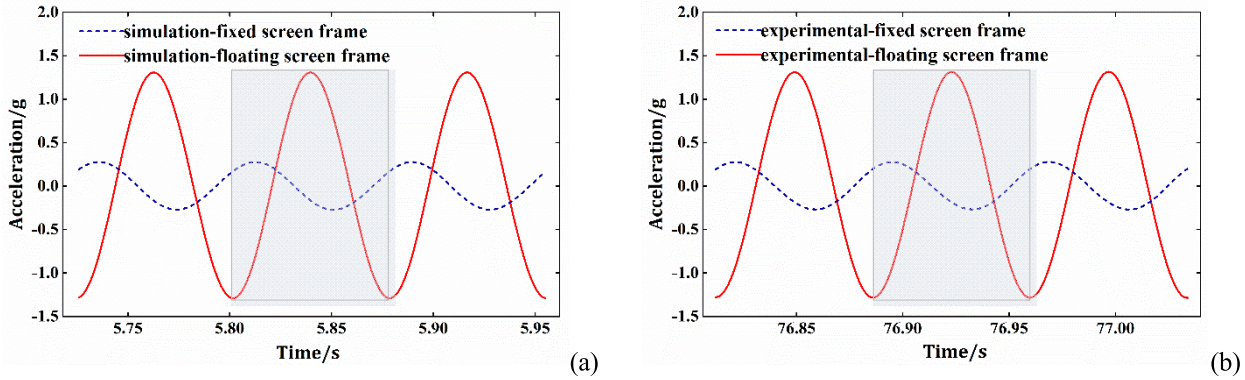


(a) Time-domain responses along x direction obtained by the simulation
(b) Time-domain responses along x direction obtained by the experiment

**FIGURE 7.** Accelerations of the flip-flow screen under the steady working condition.

### *A. RUBBER SPRINGS DAMPING EFFECTS ON RESPONSES OF THE SCREEN BODY*

According to (26), displacement differences between the two screen frames are determined by five parameters, including $\lambda$, $\alpha$, $z$, $\xi$ and $\mu$. On account of the structure of the flip-flow screen, the natural frequency ratio $\alpha$ and the mass ratio $\mu$ are constant values. Thus, displacement differences are only affected by the excitation frequency $\lambda$, damping ratio $\xi$ and relative damping $z$.

Damping effects on displacement amplitude differences between the screen frames along $x$ direction are shown in FIGURE 8. Damping ratio effects (when $z_x = 10$) are shown in FIGURE 8(a) while relative damping effects (when $\xi_x = 0.03$) are shown in FIGURE 8(b).

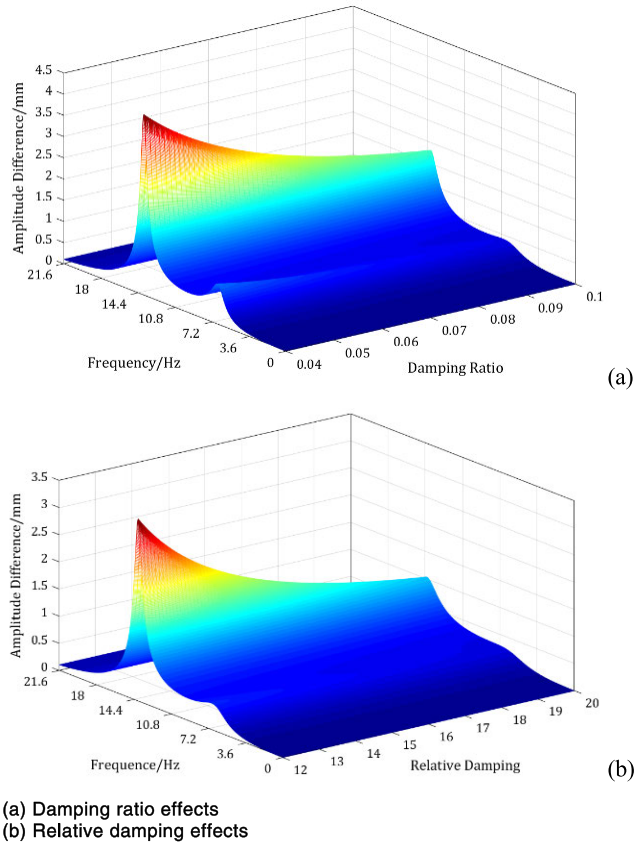


(a) Damping ratio effects
(b) Relative damping effects

**FIGURE 8.** Rubber springs damping effects on displacement amplitude differences between screen frames.

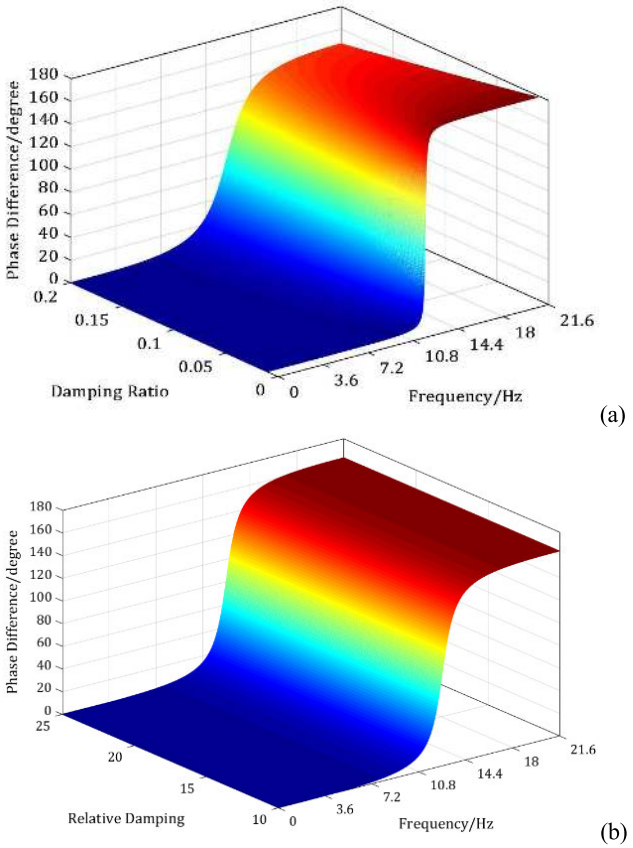


(a) Damping ratio effects
(b) Relative damping effects

**FIGURE 9.** Rubber springs damping effects on displacement phase differences between screen frames.

It can be found from FIGURE 8 that displacement amplitude differences increase rapidly in both resonance regions I and II. Thus, maximum displacement amplitude differences of the flip-flow screen are received at the first and second resonance frequencies. Moreover, with the increase of damping ratio and relative damping, the displacement amplitude differences decrease gradually. Especially in the second resonance region, the displacement amplitude differences decrease more obviously. That means small changes of damping ratio and relative damping lead to significant changes in displacement amplitude differences between screen frames when the two parameters values are rather small. Thus, the ideal displacement amplitude difference of the flip-flow screen can be easily achieved with adjustment of the damping coefficients.

Damping effects on displacement phase differences between the screen frames along $x$ direction are shown in FIGURE 9. Damping ratio effects (when $z_x = 10$) are shown in FIGURE 9(a) as relative damping effects (when $\xi_x = 0.03$) are shown in FIGURE 9(b).

As shown in FIGURE 9, with the increase of the excitation frequency, displacement phase differences increase gradually at first and the two screen frames move in the same direction. Then, after a sudden increase of the displacement phase differences, reverse movements of two screen frames exist. Theoretically, the optimal displacement phase difference during the working process is 180°, which can be obtained beyond the resonance region II. However, it can be found from FIGURE 9 that maximum phase differences are less than 180°. This demonstrates rubber springs damping reduces the maximum displacement phase difference. Moreover, as seen in FIGURE 9 (a), with the decrease of the damping ratio, maximum phase differences increase and finally toward to 180° when damping ratio goes to zero. Nevertheless, it can be illustrated from FIGURE 9 (b) that maximum phase differences are hardly influenced by relative damping, which means displacement phase differences only influenced by damping of shear springs.

In addition, when the total stiffness of shear springs in $y$ direction is twice as that in $x$ direction, the second resonance frequency of the screen along $x$ direction is broadly in line with the first resonance frequency of the screen along $y$ direction. Thus, the two screen frames move reversely along $x$ direction and vibrate in same way along $y$ direction in sub-resonance region II. At the same time the screen panel will obtain almost the maximum relaxation movement in $x$ direction accompanied by the minimum longitudinal stretch of shear springs in $y$ direction. In that case, the vibration intensity of screen surface can be improved and the longitudinal tearing of shear springs can be avoided as well.

### B. RUBBER SPRINGS DAMPING EFFECTS ON DYNAMICS OF THE SCREEN PANEL

With the load of 425.78Pa and damping coefficients of $\xi_x = \xi_y = 0.1$ and $z_x = z_y = 10$, the screen panel obtained the maximum displacement, velocity, acceleration and equivalent stress. Distribution nephograms of these dynamic parameters are shown in FIGURE 10.

The maximum deformation can be seen in the middle of the screen panel with the deflection of 26.32mm, which is larger than that of the inflexible screen panel. The maximum velocity and acceleration of the flexible screen panel are 2.194m/s and 474m/s$^2$ (i.e., 48.4g), respectively. Thus, the kinetic energy of the flip-flow screen surface is overwhelmingly higher than that of the traditional vibration screen surface, which is benefit for the process of particle penetration. According to FIGURE 10(d), the equivalent stress is evenly distributed except the two sides of the screen panel, which is about 102500Pa. For the screen panel is installed on screen frame beams, the maximum stress point, with the equivalent stress of 263200Pa, can be seen at the edges of the screen panel.

With the damping effects on screen frames responses, dynamic characteristics of the nonlinear screen panel are indirectly influenced as well. When screen panels installed in a same inclined degree, each screen panel in parallel has a similar dynamic characteristic. Thus, studies in this section based on a single screen panel can be extended to the whole screen surface.

Distributions of displacement, acceleration and equivalent stress under different damping ratio along the midsection of the screen panel are shown in FIGURE 11.

It can be discovered that the displacement distribution is symmetrical along the screen panel and the value of which decreases from the middle to the edges. Due to nonlinearity of the screen panel, there are more than one extreme points on the acceleration curve. The acceleration of the screen panel is also symmetrically distributed, and the maximum acceleration exists around half of its length. The screen panel is also covered with almost symmetrically distributed equivalent stress, and the difference of the two boundary stresses is caused by its distinct boundary responses. Besides, the equivalent stress of the rest screen panel is basically the same, just with a few regular fluctuations. Furthermore, different positions of the screen panel are affected by damping ratio in various degrees, especially the middle of the screen panel, which gained more effects from damping ratio. What we can see is that when the damping ratio equals to 0.03, the maximum acceleration of the screen panel is 39g. However, when the damping ratio increase to 0.2, the maximum acceleration declines to 32g. It follows that accelerations of the screen panel can be effectively adjusted by the damping ratio in the certain numerical interval.

Under different relative damping, distributions of displacement, acceleration and equivalent stress along the midsection of the screen panel are shown in FIGURE 12. Relative damping affects different points and different kinetic properties

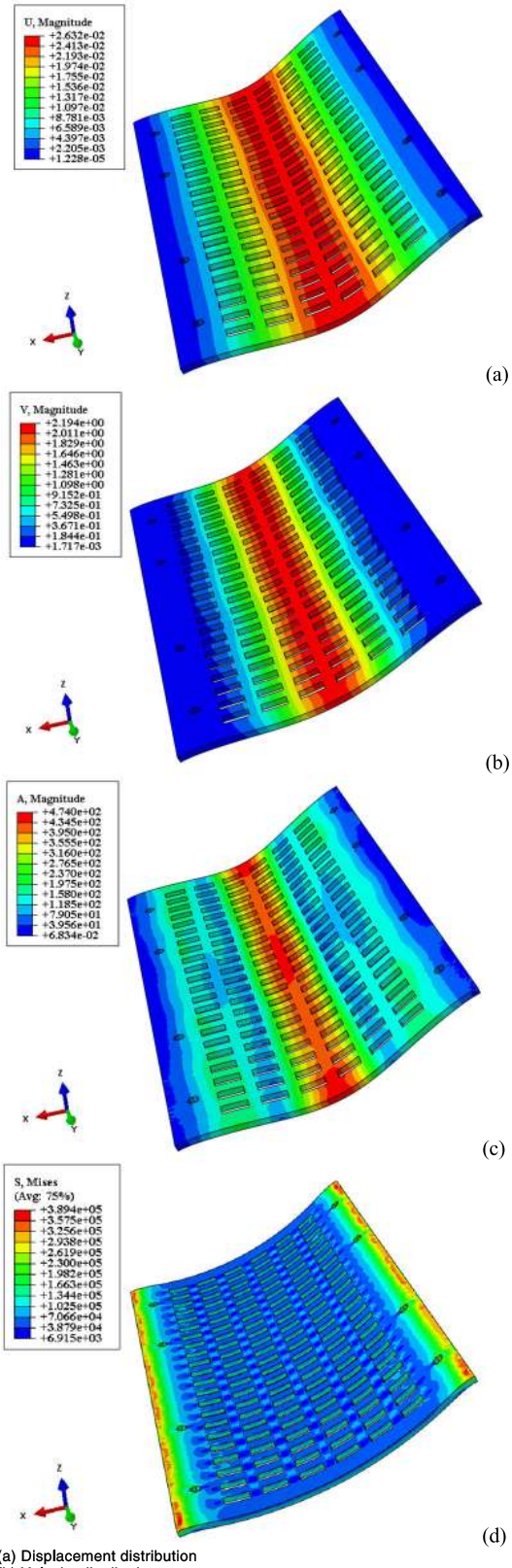


(a) Displacement distribution
(b) Velocity distribution
(c) Acceleration distribution
(d) Equivalent stress distribution

**FIGURE 10.** Distribution nephograms of the screen panel.

of the screen panel in different extends. When the relative damping is small, the influences are more obvious.

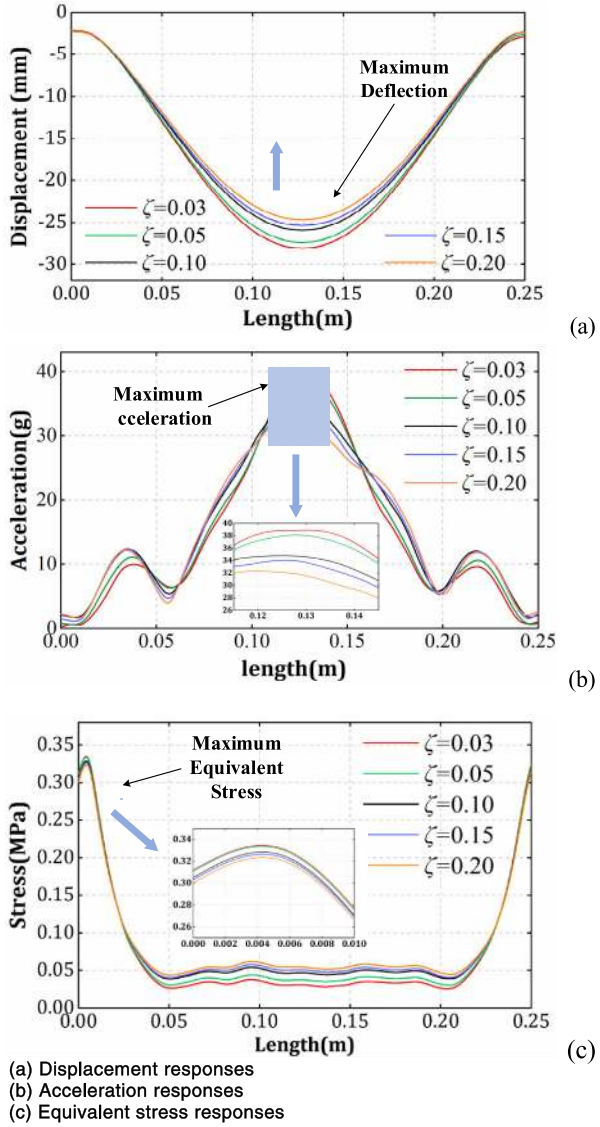


(a) Displacement responses
(b) Acceleration responses
(c) Equivalent stress responses

**FIGURE 11.** Response curves of the screen panel's midsection under different damping ratio.

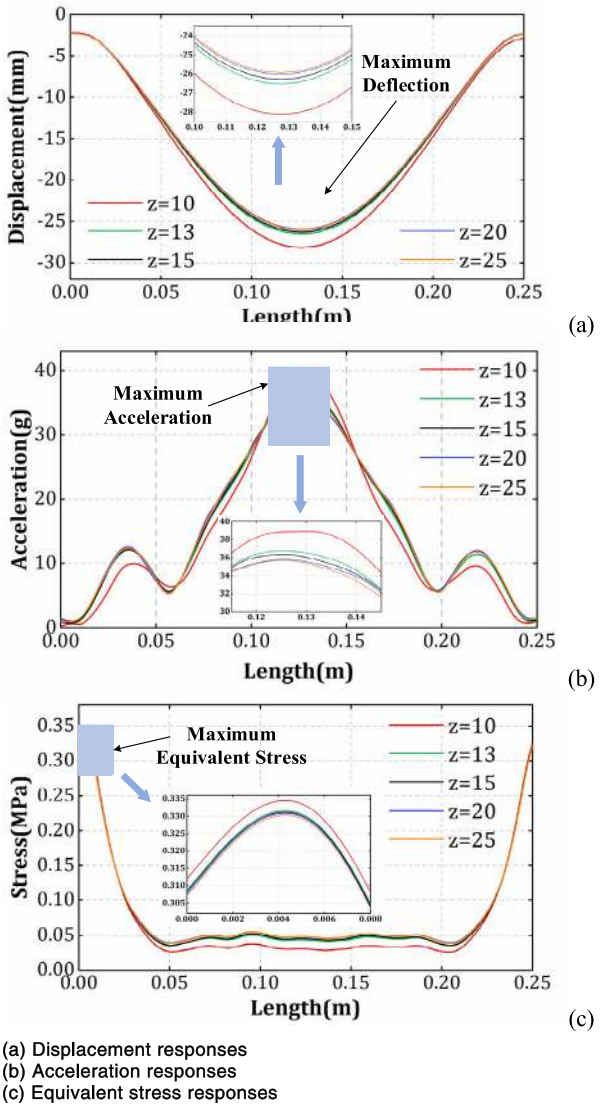


(a) Displacement responses
(b) Acceleration responses
(c) Equivalent stress responses

**FIGURE 12.** Response curves of the screen panel's midsection under different relative damping.

### C. REGRESSION ANALYSIS OF DAMPING EFFECTS

Fitting curves of maximum displacements, velocities, accelerations and equivalent stresses of the screen panel under different damping ratio and relative damping are shown in FIGURE 13 and FIGURE 14. According to several interpolation points, regression analysis between damping coefficients and dynamic properties of the screen panel are proposed.

As shown in FIGURE 13 (a), (b), and (c), negative exponential correlations exist between damping ratio and the maximum displacement, velocity, acceleration of the screen panel, respectively, which can be fitted by the nonlinear function as

$$y = y_0 + A_1 e^{-x/t_1} \tag{30}$$

where $y_0$ and $A_1$ are fitting coefficients.

Moreover, comparing with fitting curves of damping ratio in FIGURE 13, negative exponential correlations between relative damping and the maximum displacement, velocity, acceleration of screen panel (in FIGURE 14 (a), (b), and (c)) are more visible. Especially when relative damping is in the interval of [10, 15], slightly decreases of relative damping lead to dramatic increases in the maximum displacement, velocity and acceleration of the screen panel. Their exponential relations can be expressed by the following model

$$y = p_1 e^{-x/p_2} + p_3 + p_4 x \tag{31}$$

where $y_0, A_1, p_1, p_2, p_3$ and $p_4$ are fitting coefficients.

Then, the Levenberg-Marquardt method is adopted in nonlinear regression analyses. By calculating partial derivatives for each parameter to be estimated, fitting coefficients are obtained.

The maximum equivalent stress of the screen panel is in a linear correlation with both damping ratio and relative damping, which are demonstrated in FIGURE 13(d)

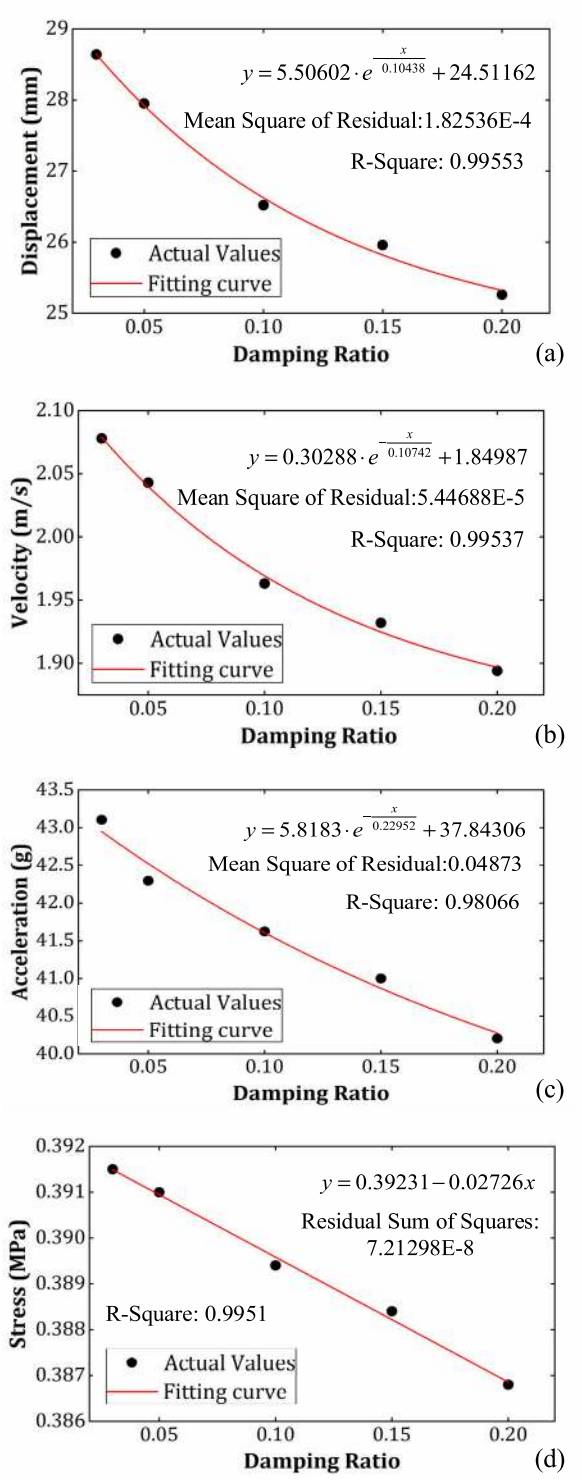


(a) Displacement regression analyses
(b) Velocity regression analyses
(c) Acceleration regression analyses
(d) Equivalent stress regression analyses

**FIGURE 13.** Nonlinear regression analyses of different damping ratio.

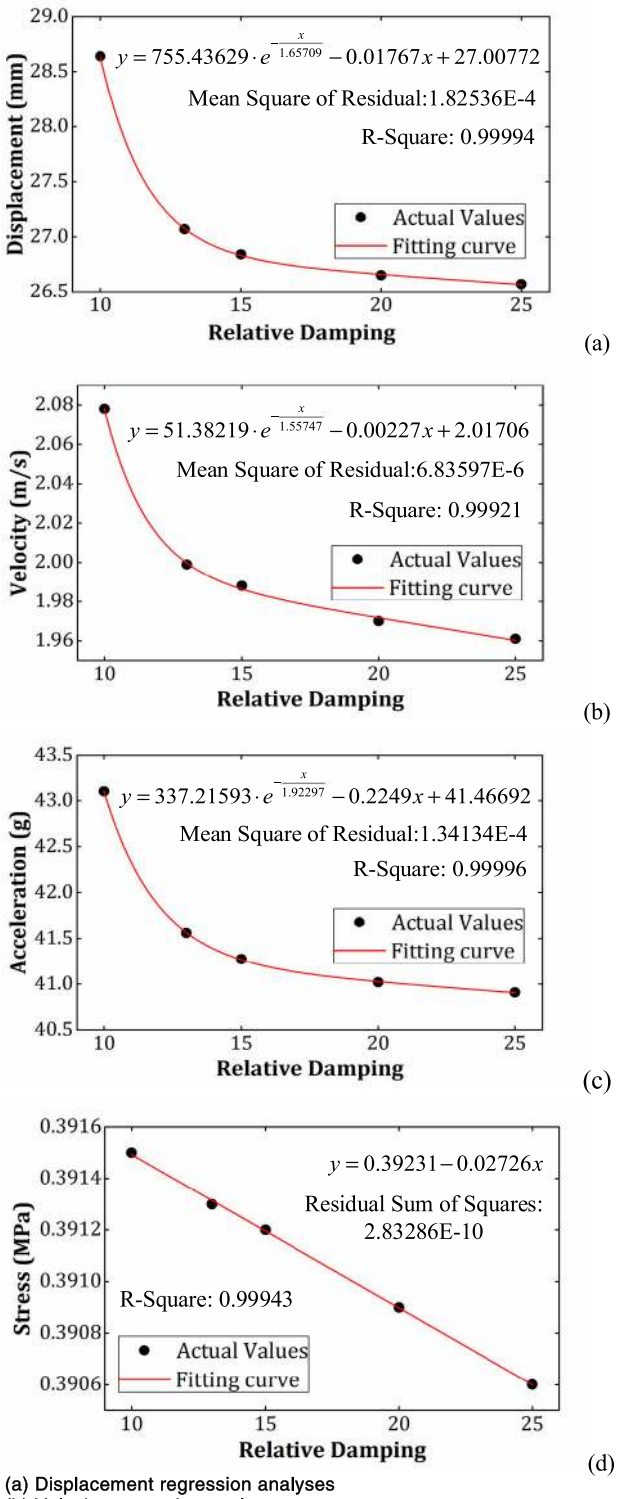


(a) Displacement regression analyses
(b) Velocity regression analyses
(c) Acceleration regression analyses
(d) Equivalent stress regression analyses

**FIGURE 14.** Nonlinear regression analyses of different relative damping.

and FIGURE 14(d). Through the least-square method, linear regression analyses are realized. Then, intercepts and slopes of linear functions are received.

The fitting precision of these models are described by R-square, RSS (residual sum of square) and MSR (Mean Square of Residua). R-square shows the goodness to fit as

RSS and MSR are used to explain the effects of variables and random errors.

$$R^2 = \frac{TSS - RSS}{TSS} = 1 - \frac{RSS}{TSS} \tag{32}$$

$$RSS = \sum_{i=1}^{n} \left(\hat{Y}_i - Y_i\right)^2 \tag{33}$$

$$MSR = reduced\ RSS = RSS\big/(n-p) = RSS\big/dof \tag{34}$$

where TSS is the total sum of square.

Obviously, R-squares of most models above are much less than 0.001, except the model of the maximum acceleration and damping ratio, which R-Square and MSR equal to 0.98066 and 0.04873, respectively. The reason can be explained for that is the variation trend of accelerations under different damping ratio are slight different to each other (as shown in FIGURE 11(b)), which affects the maximum acceleration of the screen panel and results in the low R-square value between maximum accelerations and damping ratio under the regression model.

With large R-square and small MSR or RSS values, regression models show well-fitting characteristics between damping coefficients and kinetic parameters of the screen panel. In this way, estimating values of the maximum displacement, velocity, acceleration and stress of the screen surface in the particular damping interval can be achieved.

### D. SENSITIVITY ANALYSIS OF DAMPING EFFECTS

In summary, the reduction of damping ratio and relative damping increases the acceleration and the equivalent stress of the screen surface. If the screen panel works with a reasonable acceleration, the screen performance can be optimized and the excessive stress of the screen panel is in a reliable range at the same time.

Sensitivity curves of the maximum displacement, velocity, acceleration and equivalent stress with different damping ratios and relative damping are given in FIGURE 15.

As shown in FIGURE 15(a), with the increase of damping ratio, percentage reductions of the four parameters increase. The maximum acceleration of the screen panel is the most sensitive one to the change of damping ratio while the maximum equivalent stress is in the lowest sensitivity. When damping ratio is in the range of [0.03, 0.20], percentage reductions of the maximum acceleration, velocity, displacement and stress increase monotonously. According to FIGURE 15(a), maximum percentage reductions of the maximum acceleration and the maximum equivalent stress are 11.8% and 1.2%, respectively. Therefore, damping ratio can effectively adjust the maximum acceleration of the screen panel and ensuring that the maximum stress of the screen surface is in a reasonable range concurrently.

Sensitivity curves of relative damping are given in FIGURE 15(b). With the increase of relative damping, the maximum displacement of the screen panel exhibits the highest sensitivity to the change of relative damping as the sensitivity of the maximum equivalent stress is the lowest.

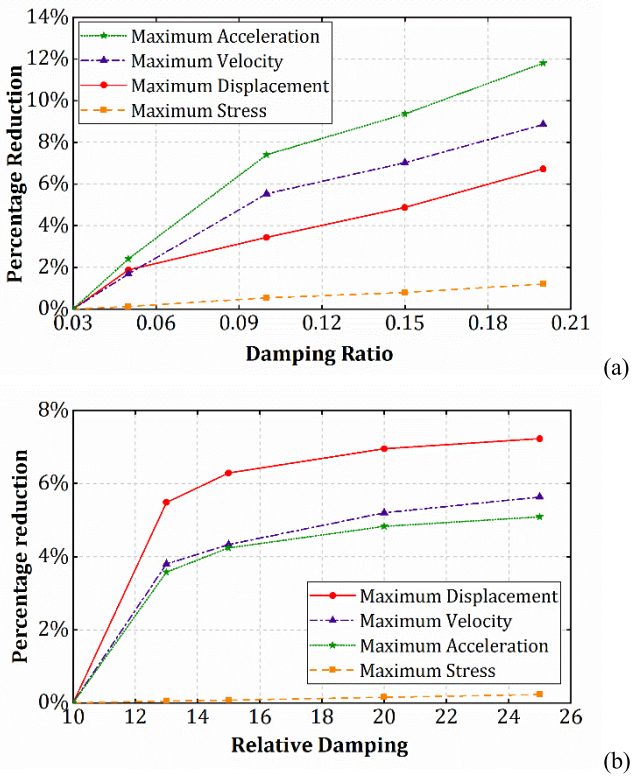


(a) Sensitivity analyses of damping ratio
(b) Sensitivity analyses of relative damping

**FIGURE 15. Sensitivity curves of damping coefficients to screen panel's kinetic parameters.**

In the interval of [10, 25] of relative damping, maximum percentage reductions of the maximum displacement, velocity and acceleration are 7.2%, 5.6% and 5.1%, respectively while that of the maximum equivalent stress is less than 0.5%. It is remarkable that when relative damping is in range of [10, 13], the maximum displacement, velocity and acceleration of the screen panel are more sensitive. That is to say, within this interval, a small decrease of relative damping can easily lead to significant increases in values of the three kinetic parameters but will not make a significant change to the equivalent stress of the screen panel.

Since the screen surface consists of several screen panels that show similar macroscopic dynamics in steady working processes, based on the above research results, the screen surface can obtain the unified and desired motions by adjusting rubber springs damping coefficients; meanwhile, due to the low sensitivity of maximum equivalent stress and the high sensitivities of maximum displacement, velocity and acceleration to rubber springs damping in the mentioned intervals, the screen surface can achieve large deflections and accelerations within small boundary stresses. Thereby, damages of the screen surface caused by large long-term boundary stresses are avoided.

## V. CONCLUSION

Using viscoelasticity of rubber spring to adjust the flip-flow screen vibration intensity is a valid solution to contradiction

between vibration strength and structural reliability. For this purpose, numerical models of the flip-flow screen under startup and shutdown modes and steady working conditions are proposed and verified. According to dynamic responses of screen frames, boundary conditions of the nonlinear screen panel are obtained. Damping influences on displacement differences between the two screen frames are studied firstly. Then, with the finite element model, effects of rubber springs damping on kinetics of the screen panel are discussed. Conclusions are drawn as follows:

(1) Displacement amplitude differences of screen frames decrease gradually with increases of damping ratio and relative damping, especially in resonance regions. But, displacement phase differences are only affected by damping ratio. With the decrease of damping ratio, maximum phase differences increase and finally toward to 180° when damping ratio goes to zero.

(2) Displacements, accelerations and stresses are symmetrically distributed along the screen panel. The maximum deformation can be seen in the middle of the screen panel with the deflection of 26.32mm, which is larger than that of the inflexible screen panel. Besides, motions of the screen panel in different positions are influenced by rubber springs damping in various degrees, especially the middle of the screen panel, which gained more effects.

(3) Negative exponential correlations exist between the maximum displacement, velocity, acceleration of the screen panel and rubber springs damping ratio, that is the same to relative damping. Moreover, the maximum stress of the screen panel is in linear correlations with both damping ratio and relative damping.

(4) The maximum acceleration of the screen panel is the most sensitive parameter to the change of damping ratio, and the maximum displacement of the screen panel shows the highest sensitivity to the change of relative damping. However, the maximum equivalent stress is in the lowest sensitivity to changes of both damping ratio and relative damping. In this way, reasonable vibration intensity of the screen surface can be achieved by adjustments of rubber springs damping coefficients.

## REFERENCES

[1] O. Makinde, B. Ramatsetse, and K. Mpofu, "Review of vibrating screen development trends: Linking the past and the future in mining machinery industries," *Int. J. Mineral Process.*, vol. 145, pp. 17–22, Dec. 2015.

[2] L. Peng, H. Jiang, X. Chen, D. Liu, H. Feng, L. Zhang, Y. Zhao, and C. Liu, "A review on the advanced design techniques and methods of vibrating screen for coal preparation," *Powder Technol.*, vol. 347, pp. 136–147, Apr. 2019.

[3] S. Baragetti and F. Villa, "A dynamic optimization theoretical method for heavy loaded vibrating screens," *Nonlinear Dyn.*, vol. 78, no. 1, pp. 609–627, Oct. 2014.

[4] C. G. Rodriguez, M. A. Moncada, E. E. Dufeu, and M. I. Razeto, "Nonlinear model of vibrating screen to determine permissible spring deterioration for proper separation," *Shock Vib.*, vol. 2016, pp. 1–7, 2016.

[5] H. Jiang, Y. Zhao, C. Duan, C. Liu, J. Wu, H. Diao, P. Lv, and J. Qiao, "Dynamic characteristics of an equal-thickness screen with a variable amplitude and screening analysis," *Powder Technol.*, vol. 311, pp. 239–246, Apr. 2017.

[6] G.-L. Gao, "A new single degree-of-freedom resonance device," *J. Central South Univ.*, vol. 19, no. 10, pp. 2782–2787, Oct. 2012.

[7] X. Xiong, L. Niu, C. Gu, and Y. Wang, "Vibration characteristics of an inclined flip-flow screen panel in banana flip-flow screens," *J. Sound Vib.*, vol. 411, pp. 108–128, Dec. 2017.

[8] H. Feng, L. Peng, R. Fang, L. Zhang, W. Ma, and X. He, "A more accurate dynamic model for dual-side excitation large vibrating screens," *J. Vibroeng.*, vol. 20, no. 2, pp. 858–871, Mar. 2018.

[9] J. Michalczyk and G. Cieplok, "Maximal amplitudes of vibrations of the suspended screens, during the transient resonance," *Arch. Mining Sci.*, vol. 61, no. 3, pp. 537–552, Sep. 2016.

[10] X. Kong, X. Zhang, X. Chen, B. Wen, and B. Wang, "Phase and speed synchronization control of four eccentric rotors driven by induction motors in a linear vibratory feeder with unknown time-varying load torques using adaptive sliding mode control algorithm," *J. Sound Vib.*, vol. 370, pp. 23–42, May 2016.

[11] L.-P. Peng, C.-S. Liu, J. Li, and H. Wang, "Static-deformation based fault diagnosis for damping spring of large vibrating screen," *J. Central South Univ.*, vol. 21, no. 4, pp. 1313–1321, Apr. 2014.

[12] C.-S. Liu, L.-P. Peng, H. Wang, and J. Li, "Fault identification for spring of large vibrating screen using free response," *Zhendong Gongcheng Xuebao/J. Vib. Eng.*, vol. 26, no. 4, pp. 624–632, Jan. 2013.

[13] L.-P. Peng, C.-S. Liu, J.-D. Wu, and S. Wang, "Stiffness identification of four-point-elastic-support rigid plate," *J. Central South Univ.*, vol. 22, no. 1, pp. 159–167, Jan. 2015.

[14] D. Tripathi, S. Pandey, and S. Das, "Peristaltic flow of viscoelastic fluid with fractional Maxwell model through a channel," *Appl. Math. Comput.*, vol. 215, no. 10, pp. 3645–3654, Jan. 2010.

[15] Z. L. and B.-Y. Xu, "Equivalent viscous damping system for viscoelastic fractional derivative mode," (in Chinese), *J. Tsinghua Univ., Sci. Technol.*, vol. 40, no. 11, pp. 27–29, Jan. 2000.

[16] R. Wang, S. Li, and S. Song, "A viscohyperelastic constitutive model for rubber used in vibration isolation," *Noise Vib. Worldwide*, vol. 38, no. 11, pp. 12–19, Dec. 2007.

[17] Y. Starosvetsky and O. Gendelman, "Dynamics of a strongly nonlinear vibration absorber coupled to a harmonically excited two-degree-of-freedom system," *J. Sound Vib.*, vol. 312, nos. 1–2, pp. 234–256, Apr. 2008.

[18] Y. Starosvetsky and O. Gendelman, "Interaction of nonlinear energy sink with a two degrees of freedom linear system: Internal resonance," *J. Sound Vib.*, vol. 329, no. 10, pp. 1836–1852, May 2010.

[19] Y. Starosvetsky and O. Gendelman, "Strongly modulated response in forced 2DOF oscillatory system with essential mass and potential asymmetry," *Phys. D, Nonlinear Phenomena*, vol. 237, no. 13, pp. 1719–1733, Aug. 2008.

[20] Y. Starosvetsky and O. Gendelman, "Vibration absorption in systems with a nonlinear energy sink: Nonlinear damping," *J. Sound Vib.*, vol. 324, nos. 3–5, pp. 916–939, Jul. 2009.

[21] S. Gong, X. Wang, and S. Oberst, "Non-linear analysis of vibrating flip-flow screens," presented at the Int. Conf. Design Manuf. Eng., 2018. [Online]. Available: https://www.researchgate.net/publication/326405216

[22] P. Balasubramanian, G. Ferrari, and M. Amabili, "Identification of the viscoelastic response and nonlinear damping of a rubber plate in nonlinear vibration regime," *Mech. Syst. Signal Process.*, vol. 111, pp. 376–398, Oct. 2018.

[23] M. Amabili, "Nonlinear damping in nonlinear vibrations of rectangular plates: Derivation from viscoelasticity and experimental validation," *J. Mech. Phys. Solids*, vol. 118, pp. 275–292, Sep. 2018.

[24] S.-P. Gong, X.-W. Wang, C. Yu, G.-F. Zhao, D.-D. Lin, N.-N. Xu, and G.-H. Zhu, "Dynamic analysis of vibrating flip-flow screen based on a nonlinear model of shear spring," (in Chinese), *J. China Coal Soc.*, vol. 44, pp. 3241–3249, Jun. 2019.

[25] B. Yuan, C. J. Xu, Z. Y. Qi, and J. F. Shi, "Transient dynamic analysis of flip-flow screen frame structure," (in Chinese), *Coal Mine Machinery*, vol. 36, no. 3, pp. 112–114, Mar. 2015.

[26] Y. Zhao, C. Liu, M. Fan, and L. Wei, "Research on acceleration of elastic flip–flow screen surface," *Int. J. Mineral Process.*, vol. 59, no. 4, pp. 267–274, Jul. 2000.

[27] C.-S. Liu and Z.-Y. Zhao, "Dynamic characteristics of flip-flow screen and screening theory," (in Chinese), *J. China Coal Soc.*, vol. 23, no. 4, pp. 92–96, Aug. 1998.

[28] L.-P. Peng, C.-S. Liu, H.-L. Dong, J. Li, and Y.-F. Xia, "Analysis and experiment on the large nonlinear deformation of a flip-flow screen," (in Chinese), *J. China Coal Soc.*, vol. 39, no. 05, pp. 976–980, May 2014.

[29] J. Zhang, Y. Huang, and Z. Chen, "The basic dynamics study of flip-flow screen and particles based on MATLAB," *Appl. Mech. Mater.*, vols. 444–445, pp. 1340–1344, Oct. 2013.
[30] X. Zhang, B. Wu, L. Niu, X. Xiong, and Z. Dong, "Dynamic characteristics of two-way coupling between flip-flow screen and particles based on DEM," (in Chinese), *J. China Coal Soc.*, vol. 44, no. 6, pp. 1930–1940, Jun. 2019.
[31] B. Wu, X. Zhang, L. Niu, X. Xiong, Z. Dong, and J. Tang, "Research on sieving performance of flip-flow screen using two-way particles-screen panels coupling strategy," *IEEE Access*, vol. 7, pp. 124461–124473, 2019.
[32] T. Belytschko, W. K. Liu, B. Moran, and K. Elkhodary, *Nonlinear Finite Elements for Continua and Structures*, 2nd ed. West Sussex, U.K.: Wiley, 2014, pp. 227–328. [Online]. Available: https://www.wiley.com/en-cn/9781118700082
[33] P. Wang, "The dynamic analysis of the inertial flip-flow screen," (in Chinese), M.S. thesis, Dept. Eng., Taiyuan Univ. Technol., Taiyuan, China, 2016.
[34] A. Oustaloup, F. Levron, B. Mathieu, and F. Nanot, "Frequency-band complex noninteger differentiator: Characterization and synthesis," *IEEE Trans. Circuits Syst. I, Reg. Papers*, vol. 47, no. 1, pp. 25–39, Jan. 2000.
[35] L. Peng, Z. Wang, W. Ma, X. Chen, Y. Zhao, and C. Liu, "Dynamic influence of screening coals on a vibrating screen," *Fuel*, vol. 216, pp. 484–493, Mar. 2018.
[36] X. Tong, X. Wu, Z. Li, and H. Xia, "DEM-FEM coupling simulations of the interactions between particles and screen surface of vibrating screen," *Int. J. Mining Mineral Eng.*, vol. 8, no. 3, pp. 250–263, 2017.

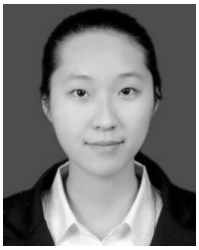

**JIAN TANG** was born in Lvliang, Shanxi, China, in 1993. She received the B.S. degree in mechanical engineering from the Taiyuan University of Science and Technology, Taiyuan, China, in 2015. She is currently pursuing the Ph.D. degree in mechanical engineering with the Taiyuan University of Technology, Taiyuan. Her research interests include mechanical dynamics analysis, dry-screening machine for moist fine coal, and application of dem analysis.

**LINKAI NIU** received the Ph.D. degree from Xi'an Jiaotong University, Xi'an, China, in 2016. He is currently a Lecturer of mechanical engineering with the Taiyuan University of Technology. He has published over 15 journals and conference papers. His research interests include dynamic modeling and vibration response mechanism of rolling bearings. He has taken charge of the China Youth Program of the National Natural Science Foundation and of Shanxi Applied Basic Research Project.

**XIAOYAN XIONG** received the Ph.D. degree from the Taiyuan University of Technology, in 2008. She is currently a Professor with the Taiyuan University of Technology. She has published over 60 journals. Her research interests span mechanical fault diagnosis, modern signal processing, and research of related software and hardware. She also hosts two national natural science projects, one project of the supported program for provincial young academic leaders, and five provincial-level projects. She is the Vice Secretary-General of the Dynamic Testing Committee of the Chinese Vibration Engineering Society and is the Chairman of the Shanxi Vibration Engineering Society.

**SHIJUN JIE** was born in Jingzhou, Hubei, China, in 1990. He received the M.S. degree in mechanical engineering from the Taiyuan University of Technology, Taiyuan, China. His research interests include dynamic analysis and design of the electromechanical system. He is a member of the Shanxi Vibration Engineering Society.